



Development of multi-directional functional near-infrared spectroscopy system for human neuroimaging studies

TAKEAKI SHIMOKAWA,^{1,3,*} TOSHIHIRO ISHII,^{2,3,4} YOICHIRO TAKAHASHI,² YUKI MITANI,² HIRONOBU MIFUNE,² SUNAO CHUBACHI,² MASAKI SATOH,² YOSHIHIRO OBA,² KAZUHIKO ADACHI,² SATORU SUGAWARA,² AND OKITO YAMASHITA¹

¹ATR Neural Information Analysis Laboratories, Kyoto 619-0288, Japan

²Research and Development Division, RICOH Company Ltd., Miyagi 981-1241, Japan

³These authors contributed equally to this work

⁴toshihiro.ishii@jp.ricoh.com

*shimokawa@atr.jp

Abstract: Multi-directional measurement using multi-directional light sources and multi-directional photodetectors drastically increases the amount of observation data without increasing the number of optical probes. In this study, we developed a novel multi-directional functional near-infrared spectroscopy (fNIRS) system for human neuroimaging studies. We tested our system by measuring the cortical hemodynamic changes of a single subject during a motor task and compared them with the same subject's functional magnetic resonance imaging (fMRI) data. We detected the direction-dependent fNIRS signals that originate from the cortical hemodynamic changes that are consistent with the fMRI data.

© 2019 Optical Society of America under the terms of the [OSA Open Access Publishing Agreement](#)

1. Introduction

Functional near-infrared spectroscopy (fNIRS) is a non-invasive imaging technique that measures oxygenated and deoxygenated hemoglobin (HbO and HbR) concentration changes that accompany neuronal activation in the cerebral cortex [1]. Compared to functional magnetic resonance imaging (fMRI), which is a large-scale imaging modality that measures the blood-oxygenation-level-dependent (BOLD) signals, fNIRS provides such advantages as safety, portability, low cost, and few physical restrictions in measurement. These merits enable anyone to be measured in natural environments: babies, elderly people, and patients with an implanted electronic device. Moreover, fNIRS can be used as a basis for a diffuse optical tomography (DOT) technique, which reconstructs three-dimensional hemodynamic images using forward light modeling, an image reconstruction algorithm, and more NIRS observation data.

With high-density NIRS probe arrays (13-mm intervals), a recent DOT study showed that cortical task-evoked activities and resting-state networks can be visualized with comparable quality to fMRI [2]. Such recent work indicates that one direction to advance the quality and the spatial resolution of fNIRS imaging techniques is to increase the amount of observation data. However, increasing the number of probes in a high-density measurement also increases the experimental workload compared with conventional low-density fNIRS studies (typically 30-mm intervals).

To solve this problem, we previously proposed a multi-directional measurement system using multi-directional sources and detectors [3]. That system drastically increased the amount of measurement data without raising the number of probes by utilizing the multiple optical paths formed in multi-directional measurements [3,4] (Fig. 1(a)). Therefore, it does not increase the experimental workload. We evaluated the previous system, which had only

single-wavelength light sources, through a phantom experiment. In this study, we developed a multi-directional and two-wavelength system applicable to human subjects and evaluated it through a human case study.

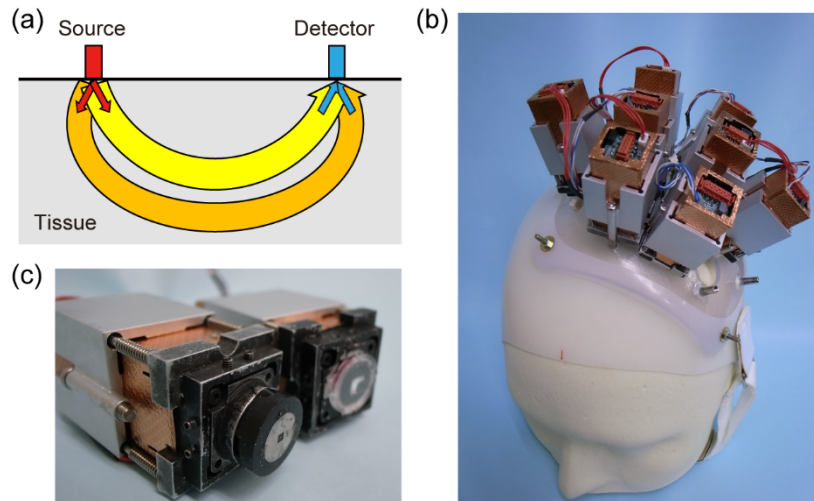


Fig. 1. (a) Conceptual diagram of multi-directional measurement. Two different optical paths exist due to different emitting and detection angles: inclined inward (yellow) and inclined outward (orange). (b) Multi-directional fNIRS system. Four source probes and four detectors were attached to head cap. (c) Enlarged view of probe tip (left: source, right: detector).

Our new multi-directional fNIRS system is shown in Fig. 1(b). Since the source and detector probes (Fig. 1(c)) emit light in four directions and also receive light from four directions, the amount of observation data is $4 \times 4 = 16$ times increased more than with a conventional single-directional fNIRS system. To test the system, we measured the left somatomotor area of a subject during a right-hand-gripping task and compared the observed multi-directional fNIRS data with fMRI data of the same subject and task. Note that our current system could not deal with the subject's hair due to its large probes and the solid, custom-made head cap in which the probes were set. In this study, we only measured one subject without hair to test the feasibility of the multi-directional fNIRS system for the first time. Note that further experiments with multiple subjects are required to evaluate its performance in human neuroimaging studies.

2. Multi-directional fNIRS system

We developed a novel fNIRS system for human neuroimaging studies. The system's schematics are given in Fig. 2. Figure 2(a) shows an overview diagram. We distributed a microcontroller unit (MCU) for each source probe and each detector probe and a master MCU controls them. The MCUs for the source probes were connected to the master MCU by an I²C bus in a daisy chain layout. The same was true for the MCUs for the detector probes. Exploded-view and cutaway drawings of the source probe are shown in Fig. 2(b). A prism and two sets of a lens and a vertical-cavity surface-emitting laser (VCSEL) comprise the optical system for a multi-directional light source (see also Fig. 2(c)). Compared with our previous single-wavelength study [3], our new system had two sets of a VCSEL and a lens for spectroscopy and used a smaller prism. The tip of the prism was covered with 2-mm aperture (Fig. 1(c)), although it is omitted in Fig. 2(b). In addition to an optical system, the source probe had printed circuit boards for a multiplexer, V/I and D/A converters, and an MCU. Figure 2(d) shows the detector probe. A lens and a photodetector, which is an array of four photodiodes, comprise the optical system for a multi-directional detector like in our previous study [3]. As well as an optical system, the detector probe had printed circuit boards for the

I/V and A/D converters and the MCU. The source and detector probes were covered with conductive material for electromagnetic shielding.

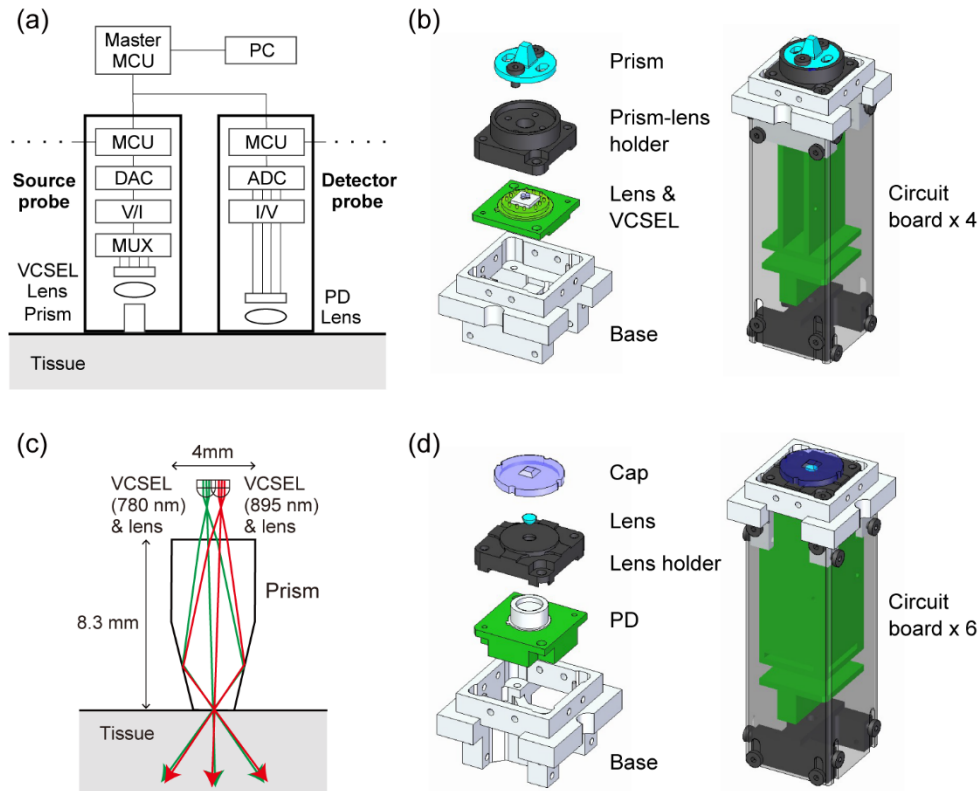


Fig. 2. Schematics of multi-directional fNIRS system. (a) Overview diagram. (b) Source probe. (c) Optical system of light-source. (d) Detector probe. VCSEL: vertical-cavity surface-emitting laser, MUX: multiplexer, PD: photodiode, V/I: V/I converter, I/V: I/V converter, DAC: D/A converter, ADC: A/D converter, MCU: microcontroller unit, PC: personal computer.

The system had four source probes and four detector probes, all of which were attached to the head cap in an experiment in a rectangular arrangement with 30-mm intervals (mean and standard deviation were $29.7 \text{ mm} \pm 1.2 \text{ mm}$). Figure 3(a) shows the probe positions and the field of view where the sum of the squared sensitivity exceeds 10^{-4} . The rectangular arrangement looks distorted due to the head curvature, and the probes are located on the scalp, whereas the field of view is depicted on the cortical surface. Figure 3(b) shows the sum of the squared sensitivity (see Section 3.3 for its calculation). Each source was designed to emit 4-way multi-directional light from the emission point to the medial, anterior, lateral, and posterior directions (azimuth angles: 0° , 90° , 180° , 270°) (Fig. 3(c)). Each detector discriminatively received light from four directions in an analogous way as the source. The actual outgoing and incoming angles are summarized below. The wavelengths of the light were 780 and 895 nm. The light's power was 1 mW, and the frame rate was 4 Hz.

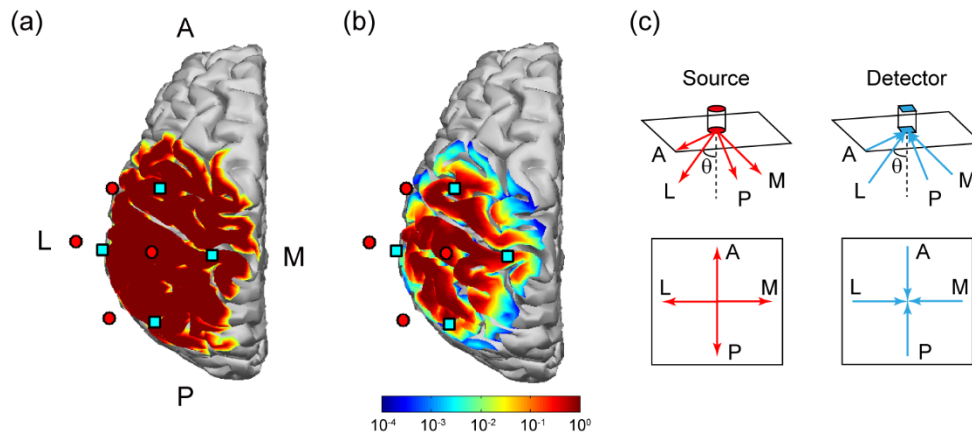


Fig. 3. Probe positions and light directions. (a) Arrangement of probes. Red circles represent sources and blue squares are detectors. Field of view is dark red. (b) Map of sensitivity magnitude. (c) Outgoing light directions from source and incoming light directions to detector. Perspective view and top view are shown. A = anterior, P = posterior, M = medial, L = lateral.

We made a calibration system and measured the emission points and the outgoing light angles of the source probes and the light-receiving characteristics of the detector probes before the experiment. We identified deviations in the emission points from the center of the prisms, depending on the probes, the light directions, and the wavelengths. The mean and standard deviation were -0.01 ± 0.39 mm in the M direction and -0.01 ± 0.40 mm in the A direction. There was no significant difference between two wavelengths ($p = 0.17$ for the M direction and $p = 0.99$ for the A direction; paired sample t-test). The mean polar angle and its standard deviation were $41.1^\circ \pm 2.1^\circ$. Here we assumed a refractive index of biological tissue as $n = 1.37$ based on previous studies [5,6] (see scalp in Table 1). The mean and standard deviation of the azimuth angle from the designated direction were $3.9^\circ \pm 3.7^\circ$. There was no significant difference between the two wavelengths ($p = 0.83$ for the polar angle and $p = 0.93$ for the azimuth angle; paired sample t-test). With respect to the detectors, there were few assembly errors because we attached them within 0.05-mm accuracy. However, they received light from a wide range of incoming angles. We measured the amount of received light giving a parallel beam at various angles. We found that they received light from polar angles $\theta = 0^\circ$ to $\theta = 30^\circ$ and the weighted average of the incoming polar angle was $\theta = 18.0^\circ$. Moreover, they received light that integrated the azimuth angle from -45° to 45° from the designated direction.

Table 1. Optical parameters of segmented head tissue

	Absorption coefficient (mm^{-1})	Scattering coefficient (mm^{-1})	Anisotropy	Refractive index
Scalp	0.019	7.8	0.89	1.37
Skull	0.019	7.8	0.89	1.37
CSF	0.004	0.009	0.89	1.37
Gray matter	0.02	9.0	0.89	1.37
White matter	0.08	40.9	0.84	1.37

3. Data acquisition and analysis

We experimentally tested our developed multi-directional fNIRS system. One right-handed male participated in the experiment. The experiment was approved by the Ethics Committee of Advanced Telecommunication Research Institute International (ATR) and the Ethics Committee of RICOH Company Ltd. The experiment was conducted in accordance with the principles of the Helsinki Declaration. Written informed consent was obtained from the participant. The subject participated in the fMRI experiment at ATR and in the fNIRS

experiment at Ricoh on different days. In both experiments, the subject was instructed to rhythmically open and close his right hand during the task period. One experimental run repeated ten trials that consisted of a 20-second pre-task rest period, a 20-second task period, and a 20-second post-task rest period. During the experiment, the subject kept his eyes closed.

3.1 fMRI data acquisition and processing

We acquired an anatomical MR image for the construction of a head model and functional images to evaluate the fNIRS data. All the MRI images were acquired on a 3T Magnetom Prisma scanner (Siemens Medical Systems, Erlangen, Germany). T1-weighted anatomical images were acquired with an MPRAGE sequence (TR = 2300 ms, TE = 2.98 ms, flip angle = 9°, inversion time = 900 ms, FOV = 256 mm, matrix = 256 × 256, voxel size = 1 × 1 × 1 mm), and functional images were acquired using an echo-planar imaging sequence (TR = 3 s, TE = 30 ms, flip angle = 80°, FOV = 192 mm, matrix = 64 × 64, voxel size = 3 × 3 × 3 mm).

We derived an activation map using the general linear model implemented in SPM8 (<http://www.fil.ion.ucl.ac.uk/spm/software/spm8/>). The image processing routine consisted of head motion correction, followed by mass-univariate linear regression, with the task–rest contrast and the head motion parameters, entered as independent variables. The resulting T-value map was thresholded ($p < 0.05$, FWE corrected) and co-registered to the subject's T1 anatomical image.

3.2 fNIRS data acquisition and processing

We conducted two experimental runs in two sessions on different days. We excluded the second run of the second session from further analysis because a large motion artifact caused more than 20% light intensity change. Therefore, we only analyzed three runs. In the experiment, the head cap was carefully placed based on the subject's nose and ears to measure the same place between sessions. The measured variability of the head cap position was around 1 to 2 mm. For the co-registration of the fNIRS data to the T1-MRI, the surface of the subject's face, three fiducial markers (nasion, left, and right preauricular points), and the positions of the probes were all acquired using a hand-held laser scanner and a stylus marker (FastSCAN Cobra; Polhemus, USA) at ATR on a different day from the fNIRS experiments.

We analyzed the fNIRS data of the nearest-neighbor source-detector pairs. The data dimension was 9 pairs × 4 directions (source) × 4 directions (detector) × 2 wavelengths = 288. The fNIRS data were preprocessed as follows. Voltage data were converted to log-ratios. A high-pass filter (Butterworth filter of order 3, cutoff 0.01 Hz) and a low-pass filter (Butterworth filter of order 7, cutoff 0.3 Hz) were applied. Each run was segmented into ten trial data sets. The baseline for each trial was adjusted so that the average during the pre-task rest period was 0. Outlier trials with a substantial deviation from the trial-median template of any measurement channel were rejected (threshold: over 5 × variance in the whole time series, number of rejected trials: 4.7 ± 2.3 trials).

We quantitatively evaluated the fNIRS data after a qualitative evaluation by applying the modified Beer-Lambert law. First, we compared the observed fNIRS data with the simulated fNIRS data based on the fMRI image. Second, we reconstructed the DOT images and compared them with the fMRI image.

3.3 Comparison with simulated fNIRS data

To quantitatively compare the fNIRS and fMRI data, we compared the observed fNIRS data with the simulated multi-directional fNIRS data based on the fMRI data. Here, the preprocessed observed fNIRS data were averaged over a time window from 25 to 45 seconds after trial onset, which is the task period considering the 5-second hemodynamic delay. We denote these as y^{obs} . In the simulation, we assumed that the cortical hemodynamic changes were proportional to the T-value map of the fMRI data and the maximum T-value

corresponds to 9 μM HbO and $-3 \mu\text{M}$ HbR concentration changes. Simulated fNIRS data \mathbf{y}^{sim} is given by the Rytov approximation [7]:

$$\mathbf{y}^{\text{sim}} = \mathbf{A}\mathbf{x}^{\text{fMRI}}, \quad (1)$$

where \mathbf{A} is the sensitivity matrix [3] and \mathbf{x}^{fMRI} is the cortical absorption changes at 780 and 895 nm due to the hemodynamic changes. We calculated the sensitivity matrix with a Monte Carlo photon migration simulator called MCX (<http://mcx.space/>) with 10^9 photons. The subject's head model was constructed by segmenting the T1 anatomical image into five tissue layers (scalp, skull, CSF, gray matter, and white matter) using FreeSurfer (<http://freesurfer.net/>). We set the same optical parameters for the tissues as in previous studies [5,6] (Table 1). The fNIRS probe positions were co-registered to the head model with an affine transformation. The measured individual variabilities of the emission points and the angles of the sources and detectors were incorporated in the photon migration simulation.

We directly compared \mathbf{y}^{sim} and \mathbf{y}^{obs} and also compared them after subtracting several factors. Here we describe the fNIRS data as $y_{p,s,d}$, where the subscripts denote the source-detector pair, the source direction, and the detector direction. The fNIRS data primarily depend on the positions of the source-detector pair. To see the direction-dependent signals, we compared them after subtracting the pair factor as $y_{s,d} = y_{p,s,d} - \bar{y}_p$, where the overline represents the average over other variables than indicated by its subscript. We also compared them after subtracting the pair and either the source or detector direction factors as $y_s = y_{p,s,d} - \bar{y}_{p,d}$ and $y_d = y_{p,s,d} - \bar{y}_{p,s}$.

3.4 DOT analysis

We reconstructed the DOT images from the fNIRS data and compared them with the fMRI T-value map. We used our previously proposed hierarchical Bayesian DOT algorithm [6,8] for solving the inverse problem. The algorithm applies a sparse-promoting prior for the cortical hemodynamic changes and a spatial smoothness prior for the scalp hemodynamic changes, based on the empirical observation that task-related cortical hemodynamics change rather locally and scalp hemodynamics change globally. Compared with the commonly used depth-compensation minimum-norm (also called spatially-variant Tikhonov regularization [2,9]), the algorithm achieved fewer false positives and improved the spatial-pattern similarity [6]. According to the algorithm, first, a provisional solution was obtained by the depth-compensation minimum-norm, whose control constant of spatially-variant regularization β was determined based on the mean value of the sensitivity for the 20-mm deep region from the surface within the fNIRS field of view [6,8]. Then the solution was used as the initial value of an iteration algorithm to refine the solution [9]. We set the confidence parameter as $\gamma_0 = 0.1 \times (\text{number of data samples})$, where the number of data samples equals the number of trials times the number of time points during the task [6]. We repeated the iteration 10,000 times. The image reconstruction area was restricted within the fNIRS field of view. Scaling factor σ was not estimated.

The reconstructed DOT images were trial-averaged and averaged over a time window from 25 to 45 seconds after the trial onset. The DOT images were compared with the fMRI T-value map. We used HbO images for the comparison. The reconstruction performance was quantified with two measures: localization error and spatial-pattern similarity. The former was computed as the distance between the center of mass of the HbO and fMRI T-value map within the fNIRS field of view. The latter was computed as Spearman's rank correlation between the HbO image and the fMRI T-value map.

4. Results

4.1 Visual inspection of fNIRS and fMRI data

First, we qualitatively evaluated the fNIRS data to see whether the system captured the cortical signals. Figure 4(a) shows the fMRI T-value map and probe positions. Figure 4(b) shows the HbO and HbR time series obtained by applying the modified Beer-Lambert law to the fNIRS data, which were averaged over the source and detector directions and trial-averaged. All three runs are shown that consist of two runs of the first session and one run of the second session. We can see typical hemodynamic change in pairs 1, 2, 3, 5, 6, and 8, and the area of the activities are consistent with the fMRI T-value map. We found no difference between the first and second session data by a visual inspection (solid and dashed lines of Fig. 4(b)), suggesting that the sensor position variability between the sessions is negligible. The result suggests the system can capture cortical hemodynamic changes.

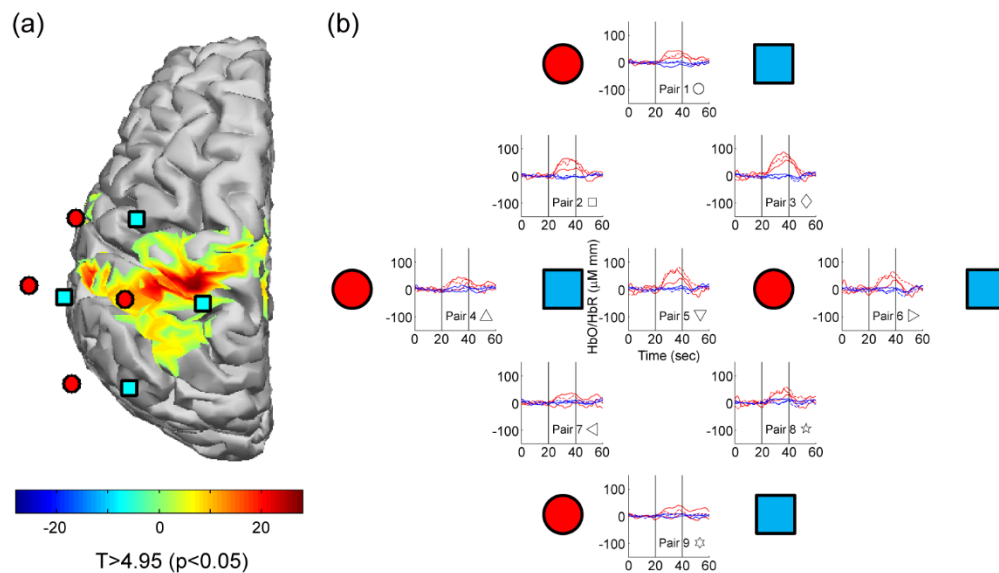


Fig. 4. Qualitative comparison of fMRI and fNIRS data. (a) fMRI T-value map. fNIRS probe positions are superimposed. (b) Trial-averaged fNIRS data. HbO (red line) and HbR (blue line) time series are plotted in each panel located on center of source-detector pairs. Data of all three runs are shown. First and second session runs are shown in solid and dashed lines. Two vertical lines inside each panel indicate task onset and offset. Symbols inside each panel are for reference in Fig. 5 to indicate each source-detector pair.

4.2 Comparison with simulated multi-directional fNIRS data

We quantitatively evaluated the multi-directional fNIRS data to determine whether the directional signals were informative or not. We simulated the multi-directional fNIRS data based on the fMRI data. The observed fNIRS data were time-averaged and averaged over all the trials and runs. Figure 5(a) shows the relationship between the simulated and observed fNIRS data. The Pearson correlation coefficient was 0.84. A high correlation value shows that the observed fNIRS data were well accounted for by the fMRI-based simulation. Next, to evaluate the direction-dependent signals, we subtracted the pair factor and compared them. Figure 5(b) shows the relationship between the simulated and observed fNIRS data after subtracting the pair factor. The Pearson correlation coefficient was 0.31. The lower correlation is due to the fact that the directional signal is as small as about one fifth of the positional factor. Nevertheless, the correlation was significant ($p = 5.7 \times 10^{-8}$; t-test), suggesting that the system detected the direction-dependent signals. Additionally, we

evaluated source directional component y_s and detector directional component y_d by subtracting the other factors and comparing the observed and simulated data. The Pearson correlation of the source directional component and the detector directional component was 0.30 and 0.35, respectively. Both correlations were significant: $p = 1.6 \times 10^{-7}$ and $p = 1.0 \times 10^{-9}$; t-test.

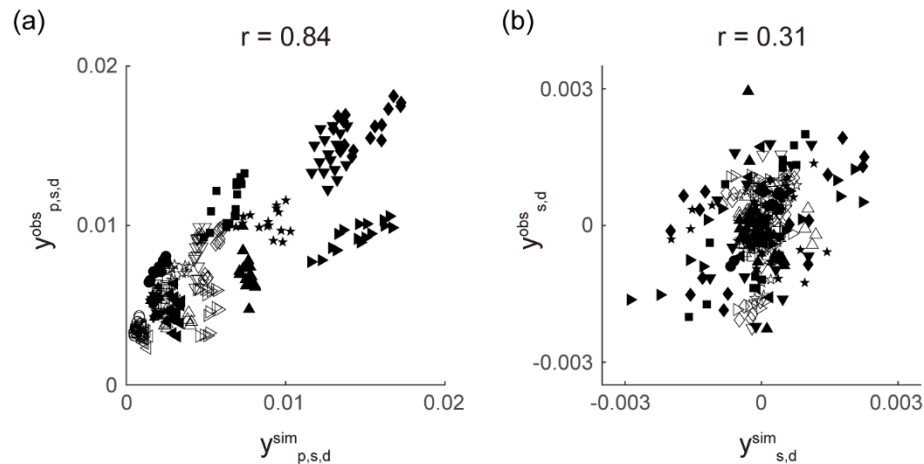


Fig. 5. Quantitative comparison of fMRI and fNIRS data. (a) Relationship between simulated and observed fNIRS data. Marker type indicates individual source-detector pair (see Fig. 4(b)). Unfilled and filled markers indicate 780- and 895-nm data. r-value indicates Pearson correlation value. (b) Relationship between simulated and observed fNIRS data after subtracting pair factor. Conventions are identical as in (a).

We extracted the pair 1 data from Fig. 5(b) and showed them in Fig. 6(a) to scrutinize the directional effect. Note that the data points are not identical because the fNIRS data in Fig. 6(a) were not averaged over runs to show the consistency between runs. Only the 895-nm data are shown. The color of the data points represents the light directions. Figure 6(b) shows the positions of the source and the detector of pair 1 and the light directions superimposed on the fMRI T-value map. Red, blue, magenta, and cyan indicate that the optical paths were biased posterior, anterior, outside of the pair, and inside of the pair by the light directions. Black indicates the other combinations of light directions. Because the main cluster of the cortical activity is located posterior and outside of the pair (Fig. 6(b)), the red and magenta signals should be large and the blue and cyan ones should be small. The simulated and observed multi-directional fNIRS data were consistent with this expectation, suggesting again that the system detected direction-dependent signals.

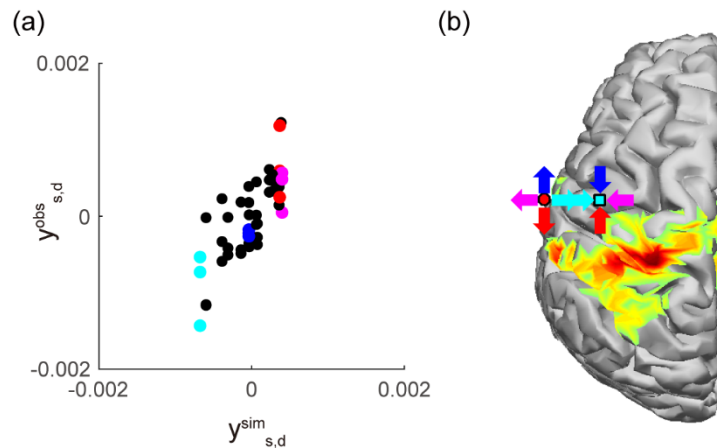


Fig. 6. Pair 1 data for explanation of direction-dependent fNIRS data in detail. (a) Relationship between simulated and observed fNIRS data after subtracting pair factor. All three runs data are shown. Color indicates pair of light directions shown in (b). Other combinations of light directions are shown in black. (b) Probe positions of pair 1 and four representative light direction pairs are indicated by colored arrows. fMRI T-value map is identical to that in Fig. 4(a).

4.3 Reconstructed DOT images

Finally, we reconstructed the DOT images by the hierarchical Bayesian DOT algorithm and compared them with the fMRI image. The hierarchical Bayesian algorithm improves the reconstructed DOT images compared with the commonly used depth-compensation minimum-norm using a sparse-promoting prior for the cortical hemodynamic changes and a spatial smoothness prior for the scalp hemodynamic changes. Figure 7 shows the reconstructed cortical HbO images of all three runs. The localization errors and the spatial-pattern similarities of the three runs were 6.0 mm, 0.47, 7.1 mm, 0.33, and 4.0 mm, 0.43. The average performance was 5.7 mm, 0.41. The localization error values were within the range of our previous high-density DOT study, where we measured the cortical hemodynamic changes during a hand-gripping task with high-density probe arrays (13-mm intervals) [6], although the spatial-pattern similarity values were lower than those of our previous high-density DOT study.

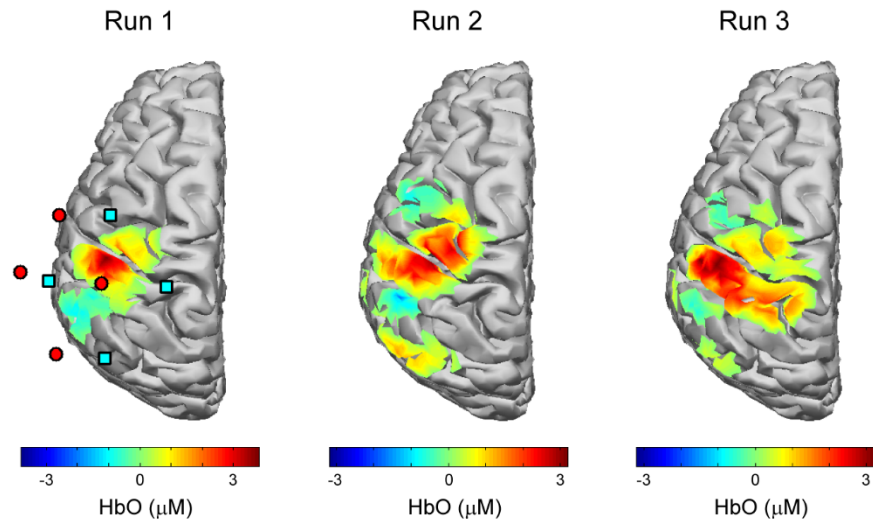


Fig. 7. Reconstructed cortical HbO images from multi-directional fNIRS data. fNIRS probe positions are superimposed on run 1's image.

Additionally, we reconstructed images by the depth-compensation minimum-norm for reference. The average performance was 5.8 mm, 0.19. The comparable localization error and lower spatial-pattern similarity were consistent with the results of our previous DOT study [6]. We also reconstructed the images by the hierarchical Bayesian DOT algorithm after averaging the fNIRS data over the source and detector directions to see the effect of the directional data. The average performance in this case was 7.9 mm, 0.40. Figure 8 compares the fMRI T-map within the field of view (red), the multi-directional DOT's HbO map (blue), and the conventional DOT's HbO map (green), where the directional fNIRS data were averaged before the image reconstruction. The HbO maps were averaged over all three runs. Although the multi-directional and conventional HbO maps almost overlap, the false positives in the anterior-lateral part of the conventional HbO map are suppressed in the multi-directional HbO map. The centers of mass of the conventional HbO maps were anteriorly biased compared with those of the fMRI T-maps and the multi-directional HbO maps in all three runs. The fact that the localization error of the multi-directional DOT decreased more than in the conventional DOT suggests that the direction-dependent data positively contributed to the estimation performance.

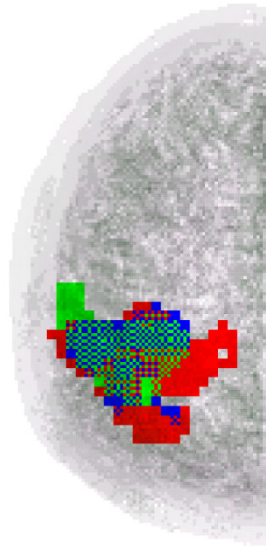


Fig. 8. Volumetric maps of fMRI T-value (red), multi-directional DOT's HbO (blue), and conventional DOT's HbO (green). Areas exceeding 20% of peak values are shown. Overlapping areas are displayed in a mosaic pattern [10]. They are overlaid on a translucent MRI anatomical image, including the scalp.

5. Discussion

We developed a novel multi-directional fNIRS system and tested it by measuring the cortical hemodynamic changes during a hand-gripping task with one subject. We compared the measured multi-directional fNIRS data with the same subject's fMRI data. After a qualitative check, we quantitatively compared the observed multi-directional fNIRS data with the simulated multi-directional fNIRS data based on the fMRI data. Analysis showed a significant correlation between the observed and simulated fNIRS signals even after we subtracted the pair position factor from them, indicating we observed the direction-dependent signals. To the best of our knowledge, this is the first detection of the direction-dependent fNIRS signals of cortical hemodynamic changes. Furthermore, we successfully reconstructed DOT images from multi-directional fNIRS data with reasonable accuracy. Although this study had only one subject and future experiments are required, these results suggest the feasibility of multi-directional fNIRS for human neuroimaging studies, which will enable us to increase the amount of measurement data without increasing the number of probes.

Even though it was statistically significant, the correlation value of the observed and simulated direction-dependent fNIRS signals was low. The primary reason is that the amplitude of the direction-dependent signals was as small as ~ 0.002 (Fig. 5(b)) and around 1/5 of the pair-position-dependent signals (Fig. 5(a)). Another reason is due to the assembly errors in the source probes. The average polar angle of the light source was 41.1° , which is larger than the detector, which was 18.0° . Therefore, the direction-dependent signals of the sources are larger than those of the detectors. However, the source directional component's correlation was lower than that of the detector directional component. This result suggests that we did not completely model the light sources; room for improving the multi-directional measurement exists by reducing the assembly errors in the source probes and more accurately modeling the light sources.

Several further studies are required for our multi-directional fNIRS system. First, a further experiment with multiple subjects is required to test whether and to what extent the multi-directional fNIRS data are beneficial for DOT image reconstruction, because DOT is a candidate for an effective way to use multi-directional fNIRS data and we cannot draw a

conclusion from the result of just one subject. Second, although our probes were large enough for simple disassembly and modification, they must be miniaturized for practical use, especially for dealing with the hair of subjects. Here we summarize the present status and the prediction ability of the probes. Both the source and the detector were 29 mm wide and weighed 50 g. We predict that the width can be reduced to 10 mm in the body and 2 mm in the portion that contacts the scalp using flexible printed circuits and smaller electronic components. The weight can be reduced to 1/3 with resin instead of metal. Therefore, we predict that the weight and the size of the probes for a multi-directional fNIRS system will resemble conventional fNIRS probes, and the multi-directional fNIRS system will be able to deal with the hair of various subjects in future studies.

Funding

The ImPACT Program of the Council for Science, Technology and Innovation (Cabinet Office, Government of Japan); National Institute of Information and Communications Technology (173, 209).

Disclosures

The authors declare that there are no conflicts of interest related to this article.

References

1. M. Ferrari and V. Quaresima, "A brief review on the history of human functional near-infrared spectroscopy (fNIRS) development and fields of application," *Neuroimage* **63**(2), 921–935 (2012).
2. A. T. Eggebrecht, S. L. Ferradal, A. Robichaux-Viehoever, M. S. Hassanpour, H. Dehghani, A. Z. Snyder, T. Hershey, and J. P. Culver, "Mapping distributed brain function and networks with diffuse optical tomography," *Nat. Photonics* **8**(6), 448–454 (2014).
3. T. Shimokawa, T. Ishii, Y. Takahashi, S. Sugawara, M. A. Sato, and O. Yamashita, "Diffuse optical tomography using multi-directional sources and detectors," *Biomed. Opt. Express* **7**(7), 2623–2640 (2016).
4. M. Hyodo, O. Matoba, S. Miyauchi, and S. Saito, "Characterization of angle-resolved measurement of diffuse reflected light," *Proc. SPIE* **10815**, 108150I (2018).
5. Q. Fang, "Mesh-based Monte Carlo method using fast ray-tracing in Plücker coordinates," *Biomed. Opt. Express* **1**(1), 165–175 (2010).
6. O. Yamashita, T. Shimokawa, R. Aisu, T. Amita, Y. Inoue, and M. A. Sato, "Multi-subject and multi-task experimental validation of the hierarchical Bayesian diffuse optical tomography algorithm," *Neuroimage* **135**, 287–299 (2016).
7. S. R. Arridge, "Optical tomography in medical imaging," *Inverse Probl.* **15**(2), R41–R93 (1999).
8. T. Shimokawa, T. Kosaka, O. Yamashita, N. Hiroe, T. Amita, Y. Inoue, and M. A. Sato, "Extended hierarchical Bayesian diffuse optical tomography for removing scalp artifact," *Biomed. Opt. Express* **4**(11), 2411–2432 (2013).
9. T. Shimokawa, T. Kosaka, O. Yamashita, N. Hiroe, T. Amita, Y. Inoue, and M. A. Sato, "Hierarchical Bayesian estimation improves depth accuracy and spatial resolution of diffuse optical tomography," *Opt. Express* **20**(18), 20427–20446 (2012).
10. T. Yoshioka, "multi_color," https://bicr.atr.jp/multi_color/.